

Real-time bioelectronic sensing of environmental contaminants

<https://doi.org/10.1038/s41586-022-05356-y>

Received: 3 September 2021

Accepted: 15 September 2022

Published online: 2 November 2022

 Check for updates

Joshua T. Atkinson^{1,2,8,10}, Lin Su^{2,3,4,9,10}, Xu Zhang², George N. Bennett^{2,5}, Jonathan J. Silberg^{2,5,6} & Caroline M. Ajo-Franklin^{2,4,7}✉

Real-time chemical sensing is crucial for applications in environmental and health monitoring¹. Biosensors can detect a variety of molecules through genetic circuits that use these chemicals to trigger the synthesis of a coloured protein, thereby producing an optical signal^{2–4}. However, the process of protein expression limits the speed of this sensing to approximately half an hour, and optical signals are often difficult to detect *in situ*^{5–8}. Here we combine synthetic biology and materials engineering to develop biosensors that produce electrical readouts and have detection times of minutes. We programmed *Escherichia coli* to produce an electrical current in response to specific chemicals using a modular, eight-component, synthetic electron transport chain. As designed, this strain produced current following exposure to thiosulfate, an anion that causes microbial blooms, within 2 min. This amperometric sensor was then modified to detect an endocrine disruptor. The incorporation of a protein switch into the synthetic pathway and encapsulation of the bacteria with conductive nanomaterials enabled the detection of the endocrine disruptor in urban waterway samples within 3 min. Our results provide design rules to sense various chemicals with mass-transport-limited detection times and a new platform for miniature, low-power bioelectronic sensors that safeguard ecological and human health.

Contamination of freshwater with natural and synthetic chemicals is a global environmental challenge¹. Of particular concern are chemicals that affect vertebrate reproduction and inorganic compounds that stimulate microbial blooms, as both can have severe ecological impacts when they enter the environment^{9–11}. Because chemical releases can be dynamic and transient, there is a need to sense these chemicals *in situ* and in real time¹¹. This sensing must also be accurate across environments with varying abiotic conditions.

Recent progress in biosensing have enabled the detection of contaminants through different modalities. Synthetic biology has produced field-deployable biosensors that monitor chemical contaminants², reporting them as visual signals^{3,4}. Alternatively, bioelectronic sensors have been developed using electroactive bacteria that couple chemical sensing to an amperometric response by producing electrical current through a process called extracellular electron transfer (EET)^{5–8,12}. These sensors all rely on the regulation of transcription for detection, which limits their response times to ≥30 min.

Engineered microorganisms have been integrated into materials to create free-standing devices for sensing diverse chemicals¹³. These approaches, which typically encapsulate bacteria in hydrogels, have produced deployable optical sensors for explosives¹⁴, heavy metals¹⁵ and chemical inducers^{16,17}. Although these materials provide mechanical integrity and support continuous sensing, they attenuate signal

transmission, which in turn degrades the signal-to-noise ratio and temporal response.

Thus, to enable real-time environmental biosensing of chemicals, we need new strategies to rapidly control and robustly transmit electrical current from microbes to electronics. Here we combine synthetic biology and materials engineering to overcome these challenges in parallel by programming a microbe to detect contaminants that trigger rapid microbial growth and impair vertebrate reproduction. These cells are interfaced with electrodes using synthetic materials to enhance the signal-to-noise of conditional EET, and we show that this bioelectronic sensor platform can detect different chemicals in urban waterway samples.

To develop a strategy to rapidly report on inorganic nutrients that trigger microbial blooms by producing a current, we designed a synthetic electron transfer (ET) pathway in *E. coli* in which sulfur oxyanions gate electron flow to an electrode. We chose to test this strategy using thiosulfate, a common dechlorination agent used in water treatment that can trigger microbial blooms when used in excess⁹. We designed a thiosulfate-dependent ET pathway using three modules (Fig. 1a). First, endogenous proteins associated with sulfur assimilation (CysP, CysM and Grx-Trx) convert thiosulfate to sulfite (Extended Data Fig. 1a), which is then used as a substrate for the input (I) module. The input module couples the reduction of sulfite to NADPH oxidation through

¹Systems, Synthetic, and Physical Biology Graduate Program, Rice University, Houston, TX, USA. ²Department of BioSciences, Rice University, Houston, TX, USA. ³State Key Laboratory of Bioelectronics, Southeast University, Nanjing, People's Republic of China. ⁴Molecular Foundry, Lawrence Berkeley National Laboratory, Berkeley, CA, USA. ⁵Department of Chemical and Biomolecular Engineering, Rice University, Houston, TX, USA. ⁶Department of Bioengineering, Rice University, Houston, TX, USA. ⁷Molecular Biophysics and Integrated Bioimaging Division, Lawrence Berkeley National Laboratory, Berkeley, CA, USA. ⁸Present address: Department of Physics and Astronomy, University of Southern California, Los Angeles, CA, USA. ⁹Present address: Yusuf Hamied Department of Chemistry, University of Cambridge, Cambridge, UK. ¹⁰These authors contributed equally: Joshua T. Atkinson, Lin Su. ✉e-mail: joff@rice.edu; cajo-franklin@rice.edu

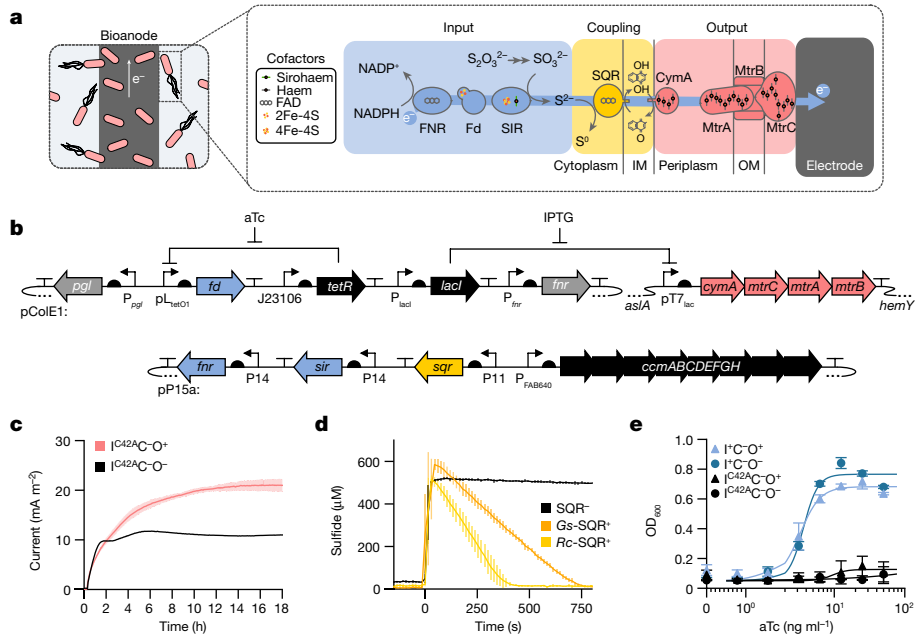


Fig. 1 | An *E. coli* sensor with a synthetic ET chain. **a**, Schematic of the sensor. Fd-dependent ET from FNR to SIR couples NADPH oxidation to sulfite reduction (input module), SQR uses sulfide oxidation to reduce quinones (coupling module) and CymA–MtrCAB use quinol oxidation to drive EET (output module). IM, inner membrane; OM, outer membrane. **b**, Schematic of the genetic circuits for expressing the different modules. **c**, Amperometric response of the BES with a working electrode poised at +0.42 V relative to a standard hydrogen electrode (V_{SHE}) containing either $\text{I}^{C42A}\text{C}^{\text{+}}\text{O}^{\text{+}}$ or $\text{I}^{C42A}\text{C}^{\text{-}}\text{O}^{\text{-}}$. Current from $\text{I}^{C42A}\text{C}^{\text{+}}\text{O}^{\text{+}}$ was significantly greater than $\text{I}^{C42A}\text{C}^{\text{-}}\text{O}^{\text{-}}$ 3 h after introduction to the BES ($P = 2.7 \times 10^{-3}$). **d**, Sulfide oxidation by $\text{I}^{C42A}\text{C}^{\text{-}}\text{O}^{\text{-}}$ cells expressing *Rc*-SQR ($370 \pm 21 \mu\text{mol s}^{-1}$) or *Gs*-SQR ($230 \pm 14 \mu\text{mol s}^{-1}$) are

significantly faster than cells lacking SQR ($5.7 \pm 1.3 \mu\text{mol s}^{-1}$) ($P = 1.75 \times 10^{-5}$ for *Rc*-SQR and 2.19×10^{-5} for *Gs*-SQR). **e**, The optical density (OD) of $\text{I}^{C^{\text{-}}}\text{C}^{\text{+}}\text{O}^{\text{+}}$ and $\text{I}^{C^{\text{-}}}\text{C}^{\text{+}}\text{O}^{\text{-}}$ cultures increase with aTc concentration. By contrast, $\text{I}^{C^{\text{-}}}\text{C}^{\text{+}}\text{O}^{\text{+}}$ and $\text{I}^{C^{\text{-}}}\text{C}^{\text{+}}\text{O}^{\text{-}}$ both present significantly higher growth complementation than $\text{I}^{C42A}\text{C}^{\text{-}}\text{O}^{\text{-}}$ and $\text{I}^{C42A}\text{C}^{\text{+}}\text{O}^{\text{+}}$ following Fd induction at $\geq 3.125 \text{ ng ml}^{-1}$ aTc ($P = 7.7 \times 10^{-4}$ for 3.125 ng ml^{-1} , $P = 1.96 \times 10^{-5}$ for 6.25 ng ml^{-1} , $P = 7.23 \times 10^{-6}$ for 12.5 ng ml^{-1} , $P = 5.68 \times 10^{-7}$ for 25 ng ml^{-1} , $P = 8.98 \times 10^{-5}$ for 50 ng ml^{-1}). Data represent the mean values, with error bars representing one standard deviation ($n = 3$ biologically independent samples). P values were obtained using two-tailed independent *t*-tests.

the expression of ferredoxin-NADP⁺ reductase (FNR), ferredoxin (Fd) and sulfite reductase (SIR). The coupling (C) module uses the product of the input module, sulfide, and a sulfide-quinone reductase (SQR), to reduce inner-membrane quinones to quinols. Lastly, the output (O) module, composed of the quinol dehydrogenase CymA and the cytochrome c-porin complex MtrCAB (CymA–MtrCAB), rapidly transfers electrons from quinols to an electrode in a thiosulfate-dependent manner using an ET pathway that requires twenty-four haem molecules, two flavin molecules, one sirohaem molecule, one 4Fe-4S cluster and one 2Fe-2S cluster.

To evaluate the performance of individual modules, we used a combination of genomic-encoded and plasmid-encoded genetic circuits that enabled plug-and-play expression of module components (Fig. 1b). The output module ($\text{O}^{\text{+}}$) was created by integrating an isopropyl β -D-1-thiogalactopyranoside (IPTG)-inducible operon that encodes CymA–MtrCAB from *Shewanella oneidensis* MR-1 into the *E. coli* genome and introducing a plasmid that constitutively expresses the cytochrome c maturation (*ccm*) operon²⁰. Strains that express components of the input ($\text{I}^{\text{+}}$) and coupling ($\text{C}^{\text{+}}$) modules were created by introducing modified *ccm* plasmids that constitutively express a subset of the input module components (FNR and SIR) and the coupling module (SQR). In addition, a second plasmid was introduced that expresses Fd using an anhydrotetracycline (aTc) inducible promoter. An ET-deficient version of the input module (I^{C42A}) was created as a negative control by generating a Cys42Ala mutant of Fd that cannot coordinate an iron-sulfur cluster²¹. To minimize off-pathway ET that competes with the desired electron flux into the input module, we used a Fd redox-insulated strain, *E. coli* EW11 (ref.²²), as our parental strain. The endogenous Fd and native SIR of this strain are deleted and replaced with the Fd-dependent input

module. Using different combinations of these plasmids (Supplementary Table 1), a set of strains (Supplementary Table 2) was constructed to evaluate the activity of the individual modules and their combinations.

To optimize the function of the output module, we assayed its expression, EET and effect on cell fitness under various induction conditions. To measure cytochrome expression, we monitored the relative red colour of cell pellets, which has previously been shown to correlate with total cytochrome concentration²⁰. To assess EET in a high-throughput manner, we measured the ability of induced cells to reduce cell-impermeable WO_3 nanorods, which change from white to blue following reduction^{23,24}. The production of the Mtr cytochromes (Extended Data Fig. 2a) and EET (Extended Data Fig. 2b) peaked between 2 and $12.5 \mu\text{M}$ IPTG. Concentrations of $> 10 \mu\text{M}$ IPTG significantly decreased $\text{I}^{C42A}\text{C}^{\text{+}}\text{O}^{\text{+}}$ growth relative to $\text{I}^{C42A}\text{C}^{\text{-}}\text{O}^{\text{-}}$ (Extended Data Fig. 2c). Thus, for all subsequent studies, we induced cells with $10 \mu\text{M}$ IPTG to maximize EET while minimizing fitness burdens. Using this optimal induction strategy, we compared $\text{I}^{C42A}\text{C}^{\text{-}}\text{O}^{\text{-}}$ and $\text{I}^{C42A}\text{C}^{\text{+}}\text{O}^{\text{-}}$ anode reduction in a bioelectrochemical system (BES), which contained M9 medium and glucose under anoxic conditions (Fig. 1c). Within 3 h, the $\text{I}^{C42A}\text{C}^{\text{+}}\text{O}^{\text{+}}$ strain produced significantly more current than the $\text{I}^{C42A}\text{C}^{\text{-}}\text{O}^{\text{-}}$ strain ($P < 0.05$), which demonstrated that the optimized output module is functional.

Our next step was to identify a SQR for the coupling module that would rapidly oxidize sulfide at the concentrations produced by the input module. The cellular activities of SQR homologues from *Rhodobacter capsulatus* (*Rc*-SQR) and *Geobacillus stearothermophilus* (*Gs*-SQR) were compared^{25,26}. When cells expressing *Rc*-SQR or *Gs*-SQR were exposed to exogenous sulfide, oxidation of $500 \mu\text{M}$ sulfide required 7 and 12.5 min , respectively (Fig. 1d). By contrast, cells lacking a SQR did not consume sulfide. When cells were labelled with

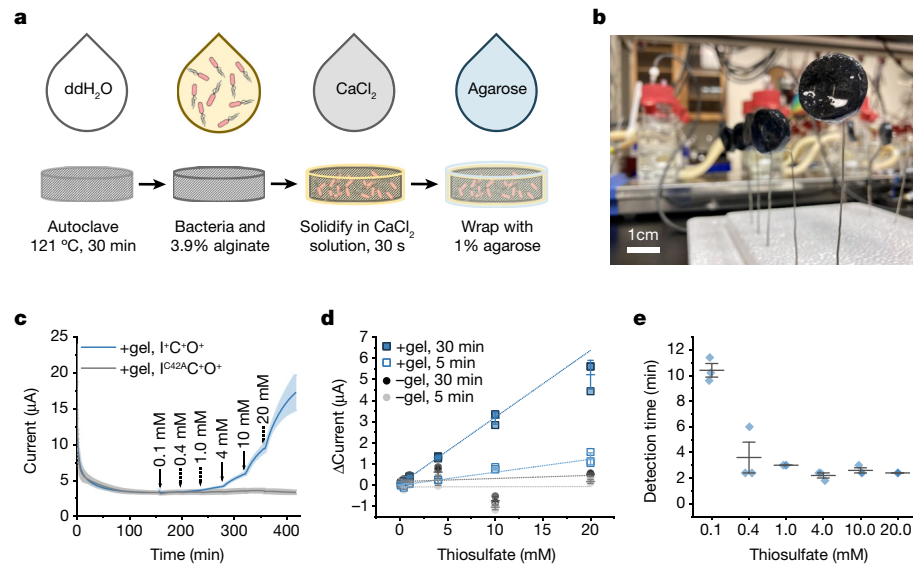


Fig. 2 | Encapsulation of a living electronic sensor enables rapid detection and quantification of thiosulfate. **a**, Schematic depicting the protocol for encapsulating the living electronic sensor with an electrode. **b**, Image of the encapsulated sensor. **c**, Amperometric response of the I⁺C⁻O⁺ and I^{C42A}C⁻O⁺ strains following exposure to increasing concentrations of thiosulfate. The working electrodes were poised at +0.42 V_{SHE}, and time zero corresponds to the start of measurements of current. **d**, The current response ($\Delta\text{Current} = I_{t(\text{injection})} - I_{t(0)}$) was calculated as the difference in current

immediately before each injection ($I_{t(0)}$) and current at a fixed time after injection ($I_{t(\text{injection})}$). Average $\Delta\text{Current}$ values are a linear function of thiosulfate concentration at 5 min ($R^2 = 0.984$) and 30 min ($R^2 = 0.994$) after thiosulfate addition. **e**, Detection time for different thiosulfate concentrations ($P \leq 0.05$). Data represent the mean values, with error bars representing one standard deviation ($n = 3$ biologically independent samples). P values were calculated using a one-way analysis of variance (ANOVA) with Tukey test.

a fluorescent probe for intracellular sulfane sulfur, an indication of SQR activity²⁷, both SQR-expressing strains accumulated significantly more sulfane sulfur than the empty vector control (Extended Data Fig. 3). Because *Rc*-SQR oxidized sulfide at faster rates, it was used as the coupling module for all subsequent studies.

Next, we investigated whether the input module acquires iron cofactors required for ET in the presence of the output module, which has a high iron cofactor demand. To that end, we measured ET mediated by the input module in the I⁺C⁻O⁺ and I⁺C⁻O⁻ strains. We leveraged a previous demonstration²¹ that growth of our parental strain can be coupled to sulfite reduction by expressing *Mastigocladus laminosus* Fd and *Zea mays* FNR and SIR. With this cellular assay, Fd-mediated ET from FNR to SIR is required to synthesize cysteine from the intermediate sulfite when sulfate or thiosulfate is provided as a sulfur source²¹ (Extended Data Fig. 1b). Intracellular sulfite transport is negatively regulated by high intracellular cysteine concentrations whereas thiosulfate transport is not (Extended Data Fig. 1c). Therefore, we chose to use thiosulfate as a substrate to support EET. Fd complementation was similar between I⁺C⁻O⁺ and I⁺C⁻O⁻ cells (Fig. 1e). This finding indicates that cells can synthesize holoproteins in the input module while expressing the output module.

We predicted the minimum thiosulfate concentration that our system could detect would have to be greater than the thiosulfate needed to meet sulfur assimilation needs such that sulfide can accumulate to supply electrons to the coupling module. *E. coli* can directly assimilate thiosulfate using the cysteine synthase CysM to produce one molecule of cysteine and one molecule of sulfite. When cysteine levels are low, sulfite is assimilated through the combined activity of FNR, Fd and SIR and the sulfide-scavenging cysteine synthase CysK (Extended Data Fig. 1a). Thus, we established the thiosulfate concentration at which cells no longer require CysK activity for growth and sulfide is free to accumulate. To that end, we evaluated growth (Extended Data Fig. 1d) and H₂S evolution (Extended Data Fig. 1e) levels of I⁺C⁻O⁻ cultures grown with different thiosulfate and Fd inducer concentrations. With ≤ 0.25 mM thiosulfate, growth of I⁺C⁻O⁻ cultures depended on Fd

expression. This result indicates that cells utilized both CysM and CysK to generate cysteine for growth (Extended Data Fig. 1a). At higher thiosulfate concentrations, cells grew to similar densities regardless of Fd expression level, which suggests that excess thiosulfate was available and cells were no longer reliant on CysK to scavenge sulfide for growth. In addition, H₂S was only observed when a concentration of > 0.5 mM thiosulfate was added. Taken together, these results suggest that ET through our full synthetic pathway should be measurable when thiosulfate is > 0.25 mM, which is lower than its concentration for toxicity in fish (4 mM)²⁸, as excess sulfide is available to be oxidized by the coupling module.

To determine whether ET through the full synthetic pathway depends on thiosulfate, we integrated all three modules together to build an I⁺C⁻O⁺ strain and measured thiosulfate-dependent EET of planktonic cells in a BES. Thiosulfate increased the current of the I⁺C⁻O⁺ strain relative to the I^{C42A}C⁻O⁺ strain (Extended Data Fig. 4), which indicated that the full pathway acts as a thiosulfate sensor. Next, to improve the low signal-to-noise, we encapsulated each strain and working electrode within an alginate–agarose hydrogel (Fig. 2a,b). Compared to planktonic cells, encapsulated cells responded to thiosulfate with a higher signal-to-noise ratio (>30-fold increase on average) (Extended Data Fig. 4b). Moreover, it exhibited a higher signal intensity (>5-fold increase), increased reproducibility (>50% decrease in standard deviation) and enhanced linearity (>10-fold increase in R^2) (Fig. 2c,d) relative to planktonic cells. This encapsulated living electronic sensor was used in all subsequent experiments.

We next probed the response of this sensor to different thiosulfate concentrations. Following the addition of 0.1 mM thiosulfate, the I⁺C⁻O⁺ strain immediately presented increased current, whereas the sensors with the I^{C42A}C⁻O⁺ strain did not respond to 20 mM thiosulfate (Fig. 2c). The current response ($\Delta\text{Current}$) of the I⁺C⁻O⁺ strain was linearly related to the thiosulfate concentration (Fig. 2d and Extended Data Fig. 5), with R^2 values of 0.984 and 0.994 for 5 and 30 min, respectively. By comparing the differences in current between the I^{C42A}C⁻O⁺ and I⁺C⁻O⁺ strains, thiosulfate was detected with $\geq 95\%$ confidence within 2–10 min

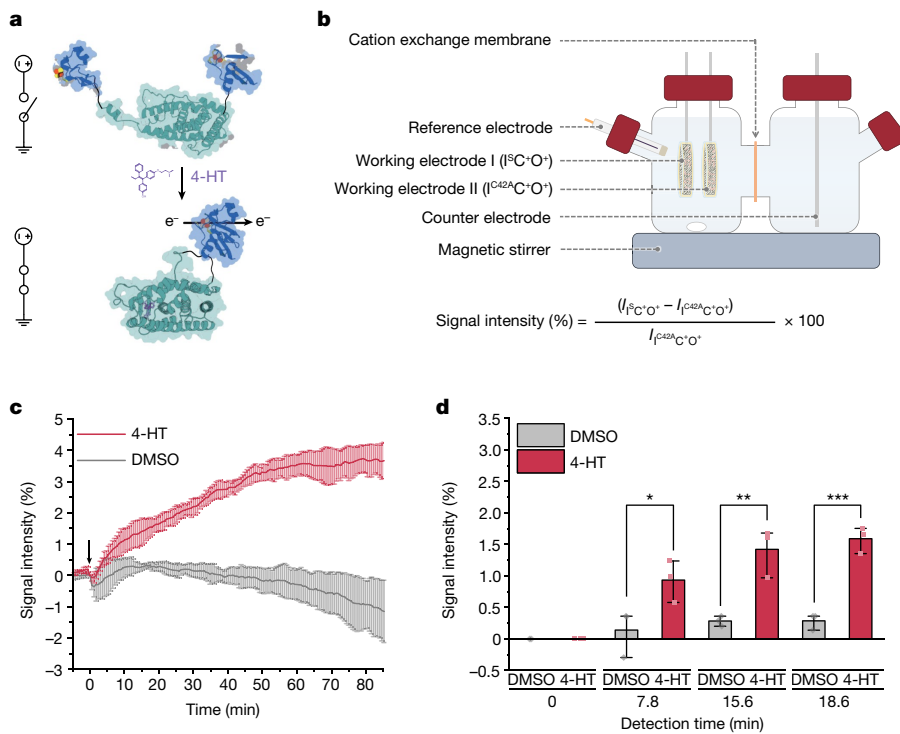


Fig. 3 | Living electronic sensors that express an electrical protein switch enable rapid detection of an endocrine disruptor. **a**, Schematic depicting an engineered Fd for which ET is regulated by 4-HT. **b**, Schematic of the 2-EWE configured BES for 4-HT sensing, which contains two working electrodes: one encapsulating the $I^{13}\text{C}^+\text{O}^-$ strain and the other containing the $I^{142}\text{C}^+\text{O}^-$ strain. **c**, Per cent increase in the amperometric response of $I^{13}\text{C}^+\text{O}^-$ relative to $I^{142}\text{C}^+\text{O}^-$ following the addition of DMSO or 4-HT in the 2-EWE configured BES, with working electrodes poised at $+0.42\text{ V}_{\text{SHE}}$. Time zero indicates 4-HT or

DMSO addition, which was approximately 95 min after the start of measuring current. **d**, Per cent increase in current of $I^{13}\text{C}^+\text{O}^-$ relative to $I^{142}\text{C}^+\text{O}^-$ at different times following the addition of DMSO or 4-HT, including 7.8 min ($P = 0.05$), 15.6 min ($P = 7.9 \times 10^{-3}$) and 18.6 min ($P = 7.8 \times 10^{-4}$), with *95%, **99% and ***99.9% confidence, respectively. Data represent the mean values, with error bars representing one standard deviation ($n = 3$ biologically independent samples). P values were calculated using one-way ANOVA with Tukey test.

of exposure (Fig. 2e). This analysis detected 0.4 mM thiosulfate in about 4 min, which is close to the estimated 0.28 mM detection limit (Supplementary Table 3 and Extended Data Fig. 5). Thus, electrical signals produced by our engineered strain enable rapid, continuous detection and quantification of thiosulfate.

To determine whether our living electronic sensor can be diversified to respond to chemicals that affect vertebrate reproduction, we leveraged Fd switches that post-translationally gate ET in response to a chemical ligand^{21,29}. To generate a switch (S) strain (Fig. 3a), designated $I^{13}\text{C}^+\text{O}^-$, we replaced the native Fd in our $I^{13}\text{C}^+\text{O}^-$ strain with an engineered Fd that contains the oestrogen receptor ligand-binding domain that transfers electrons only in the presence of oestrogen antagonists²⁹. We encapsulated the $I^{13}\text{C}^+\text{O}^-$ and $I^{142}\text{C}^+\text{O}^-$ strains into separate working electrodes and immersed them in the same anodic chamber in a two-encapsulated working electrodes (2-EWE) configuration (Fig. 3b). Dimethylsulfoxide (DMSO) or the endocrine disruptor 4-hydroxytamoxifen (4-HT) was then added to the system. To quantify changes in current induced by 4-HT in each reactor, we calculated the per cent difference in current of the $I^{13}\text{C}^+\text{O}^-$ strain relative to the $I^{142}\text{C}^+\text{O}^-$ strain as follows: signal intensity (%) = $\frac{(I^{13}\text{C}^+\text{O}^- - I^{142}\text{C}^+\text{O}^-)}{I^{142}\text{C}^+\text{O}^-} \times 100$ (Extended Data Fig. 6).

This comparison controls for any systemic environmental changes (for example, temperature, pH and carbon source) that affect the signal¹². Following 4-HT addition (12.5 μM), the signal intensity increased within a few minutes (Fig. 3c and Extended Data Fig. 6). By contrast, the chemical used to dissolve 4-HT (DMSO) did not cause detectable changes. Comparison of DMSO and 4-HT signals revealed that 4-HT was detected at 95% confidence within 7.8 min (Fig. 3d), with an increase in signal intensity of $0.93\% \pm 0.33\%$ (mean \pm s.d.). Although

the engineered Fd produced a lower signal than wild-type Fd, it enabled the detection of analytes that are not metabolic intermediates within the synthetic ET pathway. Thus, the $I^{13}\text{C}^+\text{O}^-$ living electronic sensor responds to 4-HT as designed and reduces the response time by a factor of about 4 compared with previous microbial bioelectronic sensors, which require between 0.5 and 5 h to respond to analytes^{5–8,12,30–32}.

To investigate whether our sensor functions in complex urban waterway samples, we tested our BES in riverine and marine samples spiked with thiosulfate or 4-HT. Water samples were collected from an urban beach (Galveston Beach) and two bayous (Buffalo Bayou and Brays Bayou) in the Houston Metro Area (Fig. 4a) that vary in pH, solution conductivity and organic carbon content (Fig. 4b). We first tested thiosulfate sensing using $I^{13}\text{C}^+\text{O}^-$ and $I^{142}\text{C}^+\text{O}^-$ strains in a 2-EWE configuration. In all water samples, the addition of thiosulfate (10 mM) resulted in a significant increase ($P < 0.05$) in signal intensity within 6.5 min (Fig. 4c and Extended Data Fig. 7). This result demonstrates that our 2-EWE sensor functions consistently across urban water samples with different abiotic characteristics.

As these urban water samples had poor conductivity (Fig. 4b) and abundant redox active compounds (Extended Data Fig. 8), which could interfere with bioelectronic sensing, we introduced a biocompatible and conductive $\text{TiO}_2@\text{TiN}$ nanocomposite into the encapsulation matrix (Fig. 4d). The aim was to increase the contact surface and facilitate electron transfer at the bacterial-electrode interface³³. These nanoparticle-living sensor hybrids displayed highly reproducible responses between devices, improved the signal-to-noise ratio and had a higher steady-state current in the presence of 1 mM thiosulfate (Extended Data Fig. 9). All these improvements in turn resulted in a faster response time.

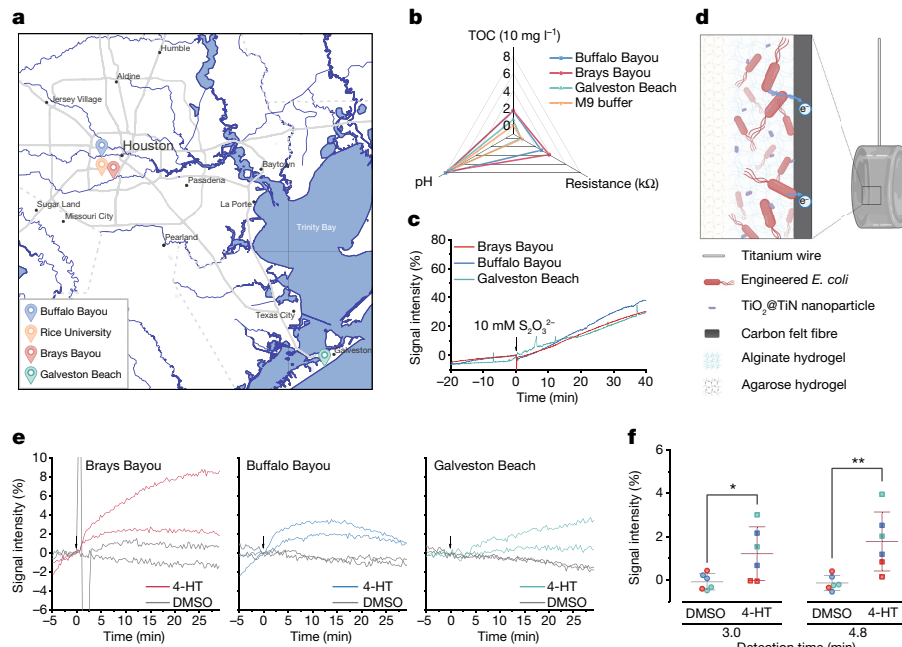


Fig. 4 | Living electronic sensors encapsulated with conductive nanoparticles enable rapid detection of pollutants in environmental samples. **a**, Map of urban waterway sampling locations in Houston, USA. **b**, pH, solution resistance and total organic carbon (TOC) measurements from each sample are compared with M9 medium. The pH ranged from 6.85 to 8.04, the solution resistance ranged from 0.044 to 3.787 kΩ and the TOC ranged from 0 to 17.05 mg l⁻¹. **c**, The per cent increase in the amperometric response of I⁵C⁺O⁺ relative to I^{42A}C⁺O⁺ following the addition of thiosulfate in a 2-EWE configured BES using each environmental sample. Data represent the values from a single experiment in each environmental sample. Time zero indicates thiosulfate addition. **d**, Scheme illustrating the encapsulation of the sensor with TiO₂@TiN nanoparticles to enhance EET efficiency. **e**, The per cent

increase in the amperometric response of I⁵C⁺O⁺ relative to I^{42A}C⁺O⁺ following the addition of either 4-HT or DMSO in a 2-EWE configured BES using each environmental sample. Time zero indicates 4-HT or DMSO addition. **f**, Detection time for 4-HT with *95% ($P = 0.034$) and **99% ($P = 7.6 \times 10^{-3}$) confidence in environmental samples. Data represent the values observed in environmental samples from Brays Bayou (red), Buffalo Bayou (blue) and Galveston Beach (green), with error bars representing the standard deviation ($n = 6$). P values were calculated using one-way ANOVA with Tukey test. Working electrodes were poised at +0.42 V_{SHE} for all amperometric experiments. The map was generated using map data sourced from the following: City of Houston, HPB, Texas Parks & Wildlife, CONANP, Esri, HERE, Garmin, Foursquare, SafeGraph, FAO, METI/NASA, USGS, EPA, NPS⁴¹.

We then used this new encapsulation approach for the detection of 4-HT in the urban water samples, using 2-EWE configurations that contained the I⁵C⁺O⁺ and I^{42A}C⁺O⁺ strains. Addition of 12.5 μM 4-HT caused immediate increases in current with I⁵C⁺O⁺ across the sampling sites, whereas DMSO caused no detectable increase (Fig. 4e). The response times for 4-HT detection were shortened to about 3 min with 95% confidence, and about 4.8 min with 99% confidence (Fig. 4f). Using a Fickian diffusion model¹⁷, we estimated the time required for 4-HT to penetrate the agarose layer and reach the bacteria (Extended Data Fig. 10). The agarose thickness varied between 1 and 2 mm, which produced a diffusional timescale between 2 and 12 min that agrees with our fastest response times. Thus, our living electronic sensor specifically detects analytes at environmentally relevant concentrations and conditions with mass-transport-limited kinetics that are up to ten times faster than the previous state-of-the-art^{5–8,12,30–32,34} (Supplementary Table 4).

This work describes three parallel innovations beyond previous work^{30–32,34} that enabled real-time sensing. First, our work introduces synthetic signal transduction using ET, in addition to phosphorylation³⁵ or proteolysis³⁶. In total, this pathway contains oxidoreductases from four different organisms across two domains of life that contain 29 cofactors. This innovation demonstrates that ET can be flexibly and extensively rewired to direct the transmission of information and energy from biology to electronics³⁶. Second, the chemical gating of EET in this work is controlled post-translationally to enable rapid response times that are well suited for the continuous monitoring of transient chemical exposures in the environment. Third, we leveraged cell encapsulation to enable ratiometric sensing, and we incorporated conductive nanomaterials³³ to improve the efficiency

of EET, both of which increased the signal-to-noise ratio and led to mass-transport-limited response times.

The living electronic sensors developed herein provide a platform that can be expanded for continuous environmental sensing. Real-time sensing requires rapid analyte detection that operates accurately for extended periods in varying environments in the absence of sample preparation. These requirements are challenging to achieve with conventional analytical approaches^{37,38} or biosensors^{2,39} that use purified proteins or nucleic acids for molecular recognition. This is because these methods rely on sample preparation, use controlled environments and are easily fouled (Supplementary Table 4). By contrast, the living electronic sensors described here detected target chemicals in real-time with limited instrumentation under various environmental conditions. To improve and customize this proof-of-concept for long-term environmental deployment, carbon sources and accessory chemicals can be incorporated within the encapsulation matrix to optimize transmission of electrical signals at the abiotic–biotic interface. Moreover, these sensors can be incorporated into devices that self-power by scavenging energy present in the environment⁴⁰. To lower the 4-HT detection limit, the extracellular ET proteins used in this pathway could be engineered into protein switches, thereby eliminating the need for analytes to enter the cell. In addition, this synthetic ET pathway could be adapted to respond under different oxygen concentrations and to various analytes in the following ways: by eliminating the ability of *E. coli* to utilize oxygen as a terminal electron acceptor; by inserting a wider range of ligand-binding domains; and by targeting different module components for switch design²¹. Small, deployable real-time bioelectronic sensors that can be distributed

across different environmental locations will revolutionize our ability to monitor chemicals as they move through ecosystems. In turn, they will inform smart sustainable practices in agriculture, mitigate the impacts of industrial waste release and ensure water security.

Online content

Any methods, additional references, Nature Research reporting summaries, source data, extended data, supplementary information, acknowledgements, peer review information; details of author contributions and competing interests; and statements of data and code availability are available at <https://doi.org/10.1038/s41586-022-05356-y>.

1. Schwarzenbach, R. P. et al. The challenge of micropollutants in aquatic systems. *Science* **313**, 1072–1077 (2006).
2. Jung, J. K. et al. Cell-free biosensors for rapid detection of water contaminants. *Nat. Biotechnol.* **38**, 1451–1459 (2020).
3. Bereza-Malcolm, L. T., Mann, G. & Franks, A. E. Environmental sensing of heavy metals through whole cell microbial biosensors: a synthetic biology approach. *ACS Synth. Biol.* **4**, 535–546 (2015).
4. Del Valle, I. et al. Translating new synthetic biology advances for biosensing into the earth and environmental sciences. *Front. Microbiol.* **11**, 618373 (2020).
5. Golitsch, F., Bücking, C. & Gescher, J. Proof of principle for an engineered microbial biosensor based on *Shewanella oneidensis* outer membrane protein complexes. *Biosens. Bioelectron.* **47**, 285–291 (2013).
6. Webster, D. P. et al. An arsenic-specific biosensor with genetically engineered *Shewanella oneidensis* in a bioelectrochemical system. *Biosens. Bioelectron.* **62**, 320–324 (2014).
7. Ueki, T., Nevin, K. P., Woodard, T. L. & Lovley, D. R. Genetic switches and related tools for controlling gene expression and electrical outputs of *Geobacter sulfurreducens*. *J. Ind. Microbiol. Biotechnol.* **43**, 1561–1575 (2016).
8. West, E. A., Jain, A. & Gralnick, J. A. Engineering a native inducible expression system in *Shewanella oneidensis* to control extracellular electron transfer. *ACS Synth. Biol.* **6**, 1627–1634 (2017).
9. Ryon, M. G., Stewart, A. J., Kszos, L. A. & Phipps, T. L. Impacts on streams from the use of sulfur-based compounds for dechlorinating industrial effluents. *Water Air Soil Pollut.* **136**, 255–268 (2002).
10. Kidd, K. A. et al. Collapse of a fish population after exposure to a synthetic estrogen. *Proc. Natl Acad. Sci. USA* **104**, 8897–8901 (2007).
11. Rice, J. & Westerhoff, P. High levels of endocrine pollutants in US streams during low flow due to insufficient wastewater dilution. *Nat. Geosci.* **10**, 587–591 (2017).
12. Zhou, A. Y., Baruch, M., Ajo-Franklin, C. M. & Mahabir, M. M. A portable bioelectronic sensing system (BESSY) for environmental deployment incorporating differential microbial sensing in miniaturized reactors. *PLoS ONE* **12**, e0184994 (2017).
13. Brooks, S. M. & Alper, H. S. Applications, challenges, and needs for employing synthetic biology beyond the lab. *Nat. Commun.* **12**, 1390 (2021).
14. Kabessa, Y. et al. Standoff detection of explosives and buried landmines using fluorescent bacterial sensor cells. *Biosens. Bioelectron.* **79**, 784–788 (2016).
15. Tang, T.-C. et al. Hydrogel-based biocontainment of bacteria for continuous sensing and computation. *Nat. Chem. Biol.* **17**, 724–731 (2021).
16. Zhao, S. et al. A new design for living cell-based biosensors: microgels with a selectively permeable shell that can harbor bacterial species. *Sens. Actuators B Chem.* **334**, 129648 (2021).
17. Liu, X. et al. Stretchable living materials and devices with hydrogel-elastomer hybrids hosting programmed cells. *Proc. Natl Acad. Sci. USA* **114**, 2200–2205 (2017).
18. Bretschger, O. et al. Current production and metal oxide reduction by *Shewanella oneidensis* MR-1 wild type and mutants. *Appl. Environ. Microbiol.* **73**, 7003–7012 (2007).
19. Jensen, H. M., TerAvest, M. A., Kokish, M. G. & Ajo-Franklin, C. M. CymA and exogenous flavins improve extracellular electron transfer and couple it to cell growth in *Mtr*-expressing *Escherichia coli*. *ACS Synth. Biol.* **5**, 679–688 (2016).
20. Goldbeck, C. P. et al. Tuning promoter strengths for improved synthesis and function of electron conduits in *Escherichia coli*. *ACS Synth. Biol.* **2**, 150–159 (2013).
21. Atkinson, J. T. et al. Metalloprotein switches that display chemical-dependent electron transfer in cells. *Nat. Chem. Biol.* **15**, 189–195 (2019).
22. Barstow, B. et al. A synthetic system links FeFe-hydrogenases to essential *E. coli* sulfur metabolism. *J. Biol. Eng.* **5**, 7 (2011).
23. Yuan, S.-J. et al. A photometric high-throughput method for identification of electrochemically active bacteria using a WO_3 nanocluster probe. *Sci. Rep.* **3**, 1315 (2013).
24. Su, L. et al. Modifying cytochrome c maturation can increase the bioelectronic performance of engineered *Escherichia coli*. *ACS Synth. Biol.* **9**, 115–124 (2020).
25. Shibata, H. & Kobayashi, S. Sulfide oxidation in gram-negative bacteria by expression of the sulfide-quinone reductase gene of *Rhodobacter capsulatus* and by electron transport to ubiquinone. *Can. J. Microbiol.* **47**, 855–860 (2001).
26. Shibata, H., Suzuki, K. & Kobayashi, S. Menaquinone reduction by an HMT2-like sulfide dehydrogenase from *Bacillus stearothermophilus*. *Can. J. Microbiol.* **53**, 1091–1100 (2007).
27. Liu, H. et al. Synthetic gene circuits enable *Escherichia coli* to use endogenous H_2S as a signaling molecule for quorum sensing. *ACS Synth. Biol.* **8**, 2113–2120 (2019).
28. Cosnefroy, A. et al. A stable fish reporter cell line to study estrogen receptor transactivation by environmental (xeno)estrogens. *Toxicol. in Vitro* **23**, 1450–1454 (2009).
29. Wu, B., Atkinson, J. T., Kahanda, D., Bennett, G. N. & Silberg, J. J. Combinatorial design of chemical-dependent protein switches for controlling intracellular electron transfer. *AIChE J.* **66**, e16796 (2020).
30. Mimee, M. et al. An ingestible bacterial-electronic system to monitor gastrointestinal health. *Science* **360**, 915–918 (2018).
31. VanArsdale, E. et al. Redox-based synthetic biology enables electrochemical detection of the herbicides dicamba and Roundup via rewired *Escherichia coli*. *ACS Sens.* **4**, 1180–1184 (2019).
32. VanArsdale, E. et al. A coculture based tyrosine-tyrosinase electrochemical gene circuit for connecting cellular communication with electronic networks. *ACS Synth. Biol.* **9**, 1117–1128 (2020).
33. Su, L., Yin, T., Du, H., Zhang, W. & Fu, D. Synergistic improvement of *Shewanella loihica* PV-4 extracellular electron transfer using a $\text{TiO}_2@\text{TiN}$ nanocomposite. *Bioelectrochemistry* **134**, 107519 (2020).
34. Terrell, J. L. et al. Bioelectronic control of a microbial community using surface-assembled electrogenic cells to route signals. *Nat. Nanotechnol.* **16**, 688–697 (2021).
35. Gordley, R. M. et al. Engineering dynamical control of cell fate switching using synthetic phospho-regulons. *Proc. Natl Acad. Sci. USA* **113**, 13528–13533 (2016).
36. Gao, X. J., Chong, L. S., Kim, M. S. & Elowitz, M. B. Programmable protein circuits in living cells. *Science* **361**, 1252–1258 (2018).
37. Smith, D. A., Sessions, A. L., Dawson, K. S., Dalleska, N. & Orphan, V. J. Rapid quantification and isotopic analysis of dissolved sulfur species. *Rapid Commun. Mass Spectrom.* **31**, 791–803 (2017).
38. Bobin-Dubigeon, C. et al. New UPLC-MS/MS assay for the determination of tamoxifen and its metabolites in human plasma, application to patients. *Future Sci. OA* **5**, FSO374 (2019).
39. Monteiro, T. & Almeida, M. G. Electrochemical enzyme biosensors revisited: old solutions for new problems. *Crit. Rev. Anal. Chem.* **49**, 44–66 (2019).
40. Reimers, C. E., Tender, L. M., Fertig, S. & Wang, W. Harvesting energy from the marine sediment–water interface. *Environ. Sci. Technol.* **35**, 192–195 (2001).
41. Esri. Community Map <https://www.arcgis.com/home/item.html?id=e64f06e8d912465a96f9ea9bfdb72676> (accessed 21 April 2021).

Publisher's note Springer Nature remains neutral with regard to jurisdictional claims in published maps and institutional affiliations.

Springer Nature or its licensor (e.g. a society or other partner) holds exclusive rights to this article under a publishing agreement with the author(s) or other rightsholder(s); author self-archiving of the accepted manuscript version of this article is solely governed by the terms of such publishing agreement and applicable law.

© The Author(s), under exclusive licence to Springer Nature Limited 2022

Article

Methods

Statistical methods were not used to predetermine sample size. Blinding and randomization were not used.

Plasmid construction

A list of all plasmids used in this study is provided in Supplementary Table 1. To enable flexibility in the use of different Fd proteins, two plasmids were used to express the input and coupling modules. The first plasmid expressed FNR, SIR, SQR and the Ccm system. The second plasmid expressed different Fd proteins (Fd, Fd(C42A) or SFd-55-ER) as well as the *E. coli* MG1655 *fnr* and *pgl* gene cassettes. These latter genes were included to improve NADPH production and defects in anaerobic respiration. The parent strain EW11 and other BL21-derived strains respond to anoxic conditions in a manner distinct from K12-derived strains such as MG1655 (ref. ⁴²). A contributing factor is a nonsense mutation in the gene encoding the fumarate and nitrate reduction regulatory protein (FNR)⁴². FNR is the global transcription factor responsible for activating the expression of fumarate and nitrate reductases as well as many other genes involved in the transition from aerobic to anaerobic metabolism⁴³. BL21-derived strains also have a deletion of the *pgl* gene, which encodes 6-phosphogluconolactonase⁴⁴. This deletion limits flux through the oxidative branch of the pentose phosphate pathway, which requires NADPH to be generated through the TCA cycle⁴⁵, transhydrogenase⁴⁶ or potentially through one-carbon metabolism⁴⁷.

The output module was chromosomally integrated. The genes encoding *R. capsulatus* and *G. stearothermophilus* SQR were obtained as Gblocks (Integrated DNA Technologies) and cloned using Golden Gate DNA assembly⁴⁸ into pSAC01 (ref. ²¹) to create pSAC01_SQR1 and pSAC01_SQR2, respectively. A constitutively expressed *ccm* operon from *E. coli* was amplified from pMO640 (ref. ²⁰) and cloned into pSAC01, pSAC01_SQR1 and pSAC01_SQR2 using Gibson DNA assembly⁴⁹ with unique nucleotide sequences (UNS3 and UNS4)⁵⁰ to generate p(e-)enzymes_NC, p(e-)enzymes_1 and p(e-)enzymes_2, respectively. The *fnr* and *pgl* gene cassettes were PCR-amplified from genomic *E. coli* MG1655 DNA and cloned into pFd007/lacI (ref. ²¹), pFd007_C42A/lacI (ref. ²¹) and pBW014 (ref. ²⁹) using Golden Gate to generate pFd007/lacI/fnr/pgl, pFd007_C42A/lacI/fnr/pgl and pERA007.55/lacI/fnr/pgl, respectively. To facilitate chromosomal integration of the output module, a T7-lac driven version of the *cymA-mtrCAB* operon from *S. oneidensis* MR-1 was PCR-amplified from p15049 (ref. ¹⁹) and cloned into pSS9 (ref. ⁵¹) using restriction enzyme cloning with KpnI and SpeI to generate pSS9:cymAmtrCAB. pSIM19 was from D. Court (NIH-National Cancer Institute). pSS9 (Addgene, plasmid 71655), pSS9-RNA (Addgene, plasmid 71656) and pX2-Cas9 (Addgene, plasmid 8581) were from R. Gill (University of Colorado). All plasmids were sequence-verified using Sanger DNA sequencing.

Strains

A list of all strains is provided in Supplementary Table 2. *E. coli* XL1-Blue (Stratgene) was used for all plasmid construction and amplification. All other experiments were performed using the *E. coli* EW11 (B-F-dcm *ompT* *hsdS(r_B-m_B-)* *gal*λ(DE3) Δ*cysI* *fpr* *ydbK* *hcr* *yeaX* *hcaD* *frdB* *hycE* *hyA* *hybC* *hyfG*)²², which was from P. Silver (Harvard University), or *E. coli* EW11-JA01 (B-F-dcm *ompT* *hsdS(r_B-m_B-)* *gal*λ(DE3) Δ*cysI* *fpr* *ydbK* *hcr* *yeaX* *hcaD* *frdB* *hycE* *hyA* *hybC* *hyfG* ss9::T7-*cymA-mtrCAB*).

To build *E. coli* EW11-JA01, CRISPR-recombineering⁵¹ was used to integrate the *cymA-mtrCAB* operon under control of the T7-lac promoter at safe-site 9 (SS9)⁵¹ in the *E. coli* EW11 genome. EW11 was made CRISPR-recombineering ready by transformation with pSIM19 (ref. ⁵²) and pX2-Cas9 (ref. ⁵¹). After selection on lysogeny broth (LB) agar plates with 50 μg ml⁻¹ kanamycin and 100 μg ml⁻¹ streptomycin at 30 °C, a fresh colony was picked and grown in 3 ml of LB with 50 μg ml⁻¹ kanamycin and 100 μg ml⁻¹ streptomycin at 30 °C for 18 h. Cultures were

diluted 1:100 into LB medium (50 ml) containing 50 μg ml⁻¹ kanamycin and 100 μg ml⁻¹ streptomycin and grown at 30 °C to exponential phase. The λ red recombination machinery was induced by incubating at 42 °C for 15 min. Cells were then concentrated (500×) and made electrocompetent by centrifugation (6,000g) and washed with 10% glycerol four times.

The T7-lac driven *cymA-mtrCAB* operon flanked by 100 bp was amplified from pSS9:cymAmtrCAB using primers JA307 (5'-CCTGAG CTTGATCCTACAC-3') and JA308 (5'-GACAGGATGATTACATAAA ATAATAGTG-3'). This linear, double-stranded DNA fragment was isolated by agarose gel extraction to obtain a substrate for CRISPR-recombineering. CRISPR-recombineering ready cells (50 μl) were electroporated with 100 ng of pSS9-gRNA and 500 ng of the T7-lac driven *cymA-mtrCAB* operon flanked by 100 bp of SS9 homology and recovered for 3 h at 30 °C in 1 ml of LB containing 0.2% arabinose, which induced Cas9 expression. Cells were then plated onto LB agar plates supplemented with 0.2% arabinose, 25 μg ml⁻¹ kanamycin and 50 μg ml⁻¹ ampicillin and grown for 18 h at 37 °C.

Integration was verified using PCR amplification of genomic DNA from the EW11 parent strain and EW11-JA01 strain purified using a Wizard Genomic DNA Purification kit (Promega). The SS9 locus was amplified using primers JA299 (5'-CATGTCGTCAAATGTTG-3') and JA300 (5'-TTGATGTTAACGTTGCAGA-3'). This ~6.7 kb band was agarose gel purified and sequence-verified using Sanger DNA sequencing with primers JA299 and JA300.

Media and cell growth conditions

All molecular biology was performed in LB medium. For growth and sulfide production assays evaluating input and coupling module functions, cells were grown in M9c or M9sa medium²¹. Colonies from freshly streaked LB agar plates were used to inoculate 1 ml of M9c with 100 μg ml⁻¹ streptomycin and 34 μg ml⁻¹ chloramphenicol in 2 ml 96-well polypropylene plates (USA Scientific, 1896-2110) and were grown at 37 °C shaking at 250 r.p.m. for 18 h. An aliquot of this culture (1 μl) was used to inoculate M9sa (100 μl) containing 100 μg ml⁻¹ streptomycin, 34 μg ml⁻¹ chloramphenicol, 10 μM IPTG and varying aTc concentrations as noted in a 96-well polystyrene plate (Corning, 3595). Cells were then grown at 37 °C, shaking at 250 r.p.m. for 24 h.

For evaluation of output module expression, EET and electrochemical assays, biomass was generated by inoculating 2×YT medium supplemented with 200 μM 8-aminolevulinic acid, 1× trace minerals, 100 μg ml⁻¹ streptomycin, 34 μg ml⁻¹ chloramphenicol with 1:100 v/v of a culture grown overnight in LB with antibiotics. Cultures were grown aerobically at 37 °C with 250 r.p.m. shaking until they reached exponential phase ($OD_{600} = 0.5 - 0.6$). To induce the expression of the *cymA-mtrCAB* operon, varying concentrations of IPTG and aTc were added as noted, and cultures were grown at 30 °C with 250 r.p.m. shaking for 18 h. The 100× trace mineral stock solution (pH 7.0) contained the following: 7.85 mM C₆H₉NO₃Na₃, 12.17 mM MgSO₄·7H₂O, 2.96 mM MnSO₄·H₂O, 17.11 mM NaCl, 0.36 mM FeSO₄·7H₂O, 0.68 mM CaCl₂·2H₂O, 0.42 mM CoCl₂·6H₂O, 0.95 mM ZnCl₂, 0.040 mM CuSO₄·5H₂O, 0.021 mM AlK(SO₄)₂·12H₂O, 0.016 mM H₃BO₃, 0.010 mM Na₂MoO₄·2H₂O, 0.010 mM NiCl₂·6H₂O and 0.076 mM Na₂WO₄·2H₂O.

Sulfide oxidation measurement

Sulfide oxidation by I⁴²A⁺O⁻ strains expressing SQRs was monitored using a sulfide-selective microsensor (SULF-MR, Unisense A/S) connected to a four-channel multiprobe micrometer (Unisense A/S). To calibrate the microsensor an eight-point standard curve was generated using a freshly prepared solution of sodium sulfide in 1× M9 salts before measurements. Cells grown to stationary phase in M9c were washed and resuspended to an $OD_{600} = 0.5$ in 1× M9 salts. This suspension (4 ml) was transferred to a respiration chamber (Unisense A/S). Following 2 min of a baseline measurement, 500 μM sodium sulfide was injected into the chamber, and sulfide was monitored every 1 s for

15 min. The mean and standard deviation of the sulfide concentration for biologically independent samples ($n = 3$) are reported. First-order rate constants were calculated using the Python package Scipy.

Bioelectrochemical analysis of output module EET

To characterize EET by the $I^{C42A}C^-O^+$ and $I^{C42A}C^-O^-$ strains, bioelectrochemistry measurements were carried out in dual-chamber (150 ml in volume per chamber) bioelectrochemical reactors (Adams & Chittenden Scientific Glass) using a VSP-300 potentiostat (BioLogic). The anodic chamber contained an Ag/AgCl reference electrode (3 M KCl, CHI111, CH Instruments) and a 6.35-mm-thick graphite felt working electrode with a 16-mm radius (Alfa Aesar). The cathodic chamber contained a 0.5-mm radius titanium wire as the counter electrode (Alfa Aesar). The two chambers were separated by a cation exchange membrane (CMI7000, Membranes International). Each chamber contained about 125 ml M9 buffer and 0.2% glucose, unless otherwise indicated. Both anodic and cathodic chambers were kept at 30 °C by placing the reactors in an incubator.

To characterize production of current by the $I^{C42A}C^-O^+$ and $I^{C42A}C^-O^-$ strains, controlled potential chronoamperometry was carried out under anoxic conditions. To maintain anoxic conditions, reactors were continuously purged with pure N₂ gas by inserting a needle into the M9 buffer for the duration of experiment. The working electrode was held at +0.42 V_{SHE} (relative to standard hydrogen electrode). Once the current was stabilized, the washed strains were inoculated into the anodic chamber with a final OD₆₀₀ of 0.5. The medium in the electrochemical chamber was mixed with a magnetic stir bar at 250 r.p.m. mixing rate for the duration of the experiment. The average current over every 36 s was recorded, and results are representative of three independent experiments, unless otherwise indicated.

Bioelectrochemical analysis of thiosulfate and 4-HT effects on EET

For bioelectronic sensing of both thiosulfate and 4-HT, bioelectrochemistry measurements were carried out in water-jacketed dual-chamber (125 ml in volume per chamber) bioelectrochemical reactors (Adams & Chittenden Scientific Glass) using a VSP-300 potentiostat (BioLogic). These measurements used the same Ag/AgCl reference electrodes (3 M KCl, CHI111, CH Instruments) and 0.5-mm radius titanium wire counter electrodes (Alfa Aesar), but smaller working electrodes (6.35-mm-thick graphite felt with a 10.5-mm radius) were used to fit the smaller reactor chambers. Each chamber contained around 115 ml M9 buffer and 0.2% glucose, unless otherwise indicated. Both anodic and cathodic chambers were kept at 30 °C by connecting the water-jackets to an ECO E4S heating circulator (Lauda-Brinkmann).

To characterize production of current by the $I^{+}C^+O^+$ and $I^{C42A}C^+O^+$ strains for thiosulfate sensing under laboratory conditions, chronoamperometry was carried out as described above. After the strains were injected and the currents stabilized, an increasing concentration of sodium thiosulfate was injected into the reactor over 40 min. The average current over every 36 s was recorded, and results are representative of three independent experiments, unless otherwise indicated. The thiosulfate-dependent ΔCurrent of the strains was calculated as the difference between the current immediately before each injection ($I_{t(0)}$) and current at a fixed time after injection ($I_{t(injection)}$). Measurements of current after 5 min and 30 min from each injection were used for linear analysis (OriginPro 2021, OriginLab) between the thiosulfate concentration and ΔCurrent.

For all 4-HT sensing, and thiosulfate sensing within environmental samples, we introduced a new 2-EWE system instead of the previous single working electrode system. The 2-EWE system included two types of strains ($I^{+}C^+O^+$ and $I^{C42A}C^+O^+$ strains for 4-HT sensing, or $I^{+}C^+O^+$ and $I^{C42A}C^+O^+$ strains for thiosulfate sensing) encapsulated separately with the working electrodes in the same reactor chamber, which generated two signals of current under the same environmental conditions simultaneously by connecting to two potentiostat channels. The potentiostat

was operated under a ‘counter electrode to ground’ mode by connecting one shared counter electrode, which was grounded, one shared reference electrode and two individual working electrodes. During the test, there were also some changes to mimic the practical biosensing scenario: river or marine water was filtered with a 0.22-μm filter and then used in the reactors as electrolyte without any additives; the needle for purging N₂ gas was lifted immediately above the liquid level after working electrodes were introduced to minimize the disturbance from purging; magnetic stirring was also stopped for the same purpose; for 4-HT or DMSO sensing, 10 mM sodium thiosulfate and 0.2% glucose were also included in the M9 buffer solution. For increased resolution, the average current over every 3.6 s was recorded, and results are representative of three independent experiments, unless otherwise indicated.

As described above, the 2-EWE system allows measurement of signals of current from two different strains at the same time and condition. By comparing the difference between these two signals, any other systemic effects (such as changes in temperature, pH, carbon source, among others) can be excluded, such that the signal represents our designed ET (that is, the response to only 4-HT or thiosulfate). Currents are reported as the per cent change between the sensing ($I^{+}C^+O^+$) and the control ($I^{C42A}C^+O^+$) strains:

$$\text{Signal intensity (\%)} = \frac{(I^{+}C^+O^+ - I^{C42A}C^+O^+)}{I^{C42A}C^+O^+} \times 100$$

Cell encapsulation

Concentrated washed strains (OD₆₀₀ = 40) and sodium alginate solution (3.9 wt%, in M9) were mixed at a 1:1 ratio on ice. The mixture (1 ml) was applied to a carbon felt electrode (10.5 mm radius) at room temperature, and it was solidified by immersing into CaCl₂ aqueous solution (3 wt%) for 30 s. The residual chemicals on the hydrogel–electrode surface were washed with M9 medium. Subsequently, the formed hydrogel was covered with 1 wt% agarose to provide mechanical support. The encapsulated devices contained approximately 2×10^{10} cells.

The TiO₂@TiN nanocomposite was synthesized as previously reported³³. In brief, TiO₂ nanoparticles (P25, Alfa Aesar) were heated at 900 °C in a tube furnace (KTL1400, Nanjing University Instrument Plant) in an ammonia atmosphere for 2 h. When mixing with the strains and sodium alginate solution, 1 mg ml⁻¹ TiO₂@TiN nanocomposite was added.

Water sampling and characterization

The environmental samples were collected from the Houston area and stored at 4 °C. Before measurement, all environmental samples were filtered with 0.2-μm sterile membranes to remove solids and microorganisms. The pH of each sample was measured with a pH meter (F20, Mettler Toledo). Resistance was measured by electrochemical impedance spectroscopy using a three-electrode system in 125 ml dual-chamber reactors, with an amplitude of 5 mV over a frequency range of 100 kHz to 0.01 Hz at open circuit potential. The results were analysed with ZView 3.5b (Scribner Associates). Total organic carbon (TOC) analysis was conducted using a TOC-vcsh analyser (Shimadzu). Cyclic voltammetry was performed using a VSP-300 potentiostat (BioLogic) and scanned from −0.8 V to 0.6 V versus Ag/AgCl, and the scan rate was 10 mV s⁻¹.

Cytochrome expression and function analysis

After growth in 96-well plates, 150 μl of culture was pelleted in white, U-bottom 96-well polystyrene plates (Corning, 3917). Before pelleting, the cells were washed and resuspended in anoxic M9 minimal medium supplemented with 100 mM sodium lactate. Additionally, 3 mg ml⁻¹ WO₃ nanoparticles were added and incubated under anoxic conditions for 6 h at 30 °C before pelleting to evaluate EET. To evaluate redness

Article

and blueness for each assay, the plates containing the cell pellets were scanned using a desktop scanner. Regions of interest from each pellet were identified using the Matlab (R2018a) ImageProcessing toolbox (MathWorks). The relative red intensity was calculated by taking the ratio intensity in the red channel (I_{red}) to the greyscale intensity (I_{grey}), red intensity = $(I_{\text{red}})/(I_{\text{grey}})$. The relative blue intensity was calculated by taking the ratio of the intensity in the blue channel (I_{blue}) to the greyscale intensity (I_{grey}), blue intensity = $(I_{\text{blue}})/(I_{\text{grey}})$. For blue intensity analysis, WO_3 oxide nanoparticles were synthesized as previously described²⁴. In brief, 0.85 g $\text{Na}_2\text{WO}_4 \cdot 2\text{H}_2\text{O}$ and 0.29 g NaCl were dissolved in 20 ml ddH₂O, then pH was adjusted to 2.0 with 3 M HCl. The solution was transferred into a hydrothermal reactor and heated at 180 °C for 7 h. WO_3 nanoparticles were then collected by washing with ddH₂O until the supernatant reached pH 7.0; the solid was collected by filtering through a 0.45-μm membrane.

Sulfane sulfur analysis

To measure intracellular sulfur accumulation following sulfide oxidation by SQR, a fluorescent probe for sulfane sulfur was used as previously described²⁷. Cells were washed two times in 50 mM HEPES (pH 7.4) and resuspended to OD₆₀₀ = 2 in HEPES buffer containing 10 μM SSP4 (3',6'-di(O-thiosalicyl)fluorescein, Dojindo Laboratories) and 0.5 mM dodecyltrimethylammonium bromide. Cells were incubated for 15 min at 37 °C in the dark with gentle shaking (150 r.p.m.) and washed two times with HEPES buffer. OD₆₀₀ and fluorescence intensity ($\lambda_{\text{excitation}} = 482 \text{ nm}$, bandwidth = 20 nm; $\lambda_{\text{emission}} = 515 \text{ nm}$, bandwidth = 20 nm) were quantified using a Spark microplate reader (Tecan). The mean and standard deviation of the OD-normalized fluorescence intensity for biologically independent samples ($n = 3$) are reported.

Hydrogen sulfide production

Evolution of H₂S(g) from cultures was monitored using a semiquantitative lead acetate filter paper assay that monitors the formation of insoluble PbS pigment in 96-well plates⁵³. Whatman no.1 filter paper was cut to fit inside the lid of a 96-well plate (Costar, 3526). A 2% lead acetate solution in water was prepared, and particulates were removed by filtration through a 0.22-μm filter. The cut filter paper was then soaked in 2% lead acetate for 30 min. Filter paper was removed and allowed to air dry overnight. Dried filter papers were applied to the inside of the 96-well plate before growth experiments. Following incubation with cultures in the plates, the filter paper was scanned, and the intensity of the grey channel was quantified using the Fiji image processing package with the ReadPlate3 plugin (<https://sites.imagej.net/ReadPlate/plugins/>). The mean and standard deviation of the grey channel intensity for biologically independent samples ($n = 3$) are reported.

Calculation of diffusional timescale

To estimate the time required for analytes, such as 4-HT or thiosulfate, to reach the encapsulated *E. coli*, we calculated the diffusional timescale following a previously described model¹⁷. This model assumes an initial concentration of analyte, I_0 , is separated by a cell-free hydrogel layer of thickness, L , from the bacteria (Extended Data Fig. 10). This model determines the time for the analyte concentration to reach K , the minimum analyte concentration needed to generate a response, at position L using an approximate solution to Fick's Law in 1D:

$$t_{\text{diffuse}} \approx \frac{4}{9} \frac{1}{\left(\frac{I_0}{K} - 1\right)^{0.56}} \frac{L^2}{D_g}$$

As the diffusion coefficient of small molecules in agarose is typically about 95% of that in water⁵⁴, and the diffusion coefficient of 4-HT in water (D_{water}) is $6.6 \times 10^{-10} \text{ m}^2 \text{ s}^{-1}$, we set $D_g = D_{\text{water}} \times 0.95 = 6.3 \times 10^{-10} \text{ m}^2 \text{ s}^{-1}$. We set K and I_0 equal to 0.1 mM (Fig. 2) and 10 mM, respectively. Owing to our fabrication process, L was not stringently controlled and varied

between 1 and 3 mm. As t_{diffuse} depends on L^2 , this variability translated into a significant variation in the critical diffusion timescale, producing an estimated t_{diffuse} between 1 and 8 min.

Statistics

All reported *P* values were obtained using two-tailed, independent *t*-tests or one-way analysis of variance using Tukey's test as noted. Sample sizes were in accordance with community standards.

Estimating the detection limit for thiosulfate sensing

In the case of thiosulfate sensing, the detection limit (DL) was estimated following the ICH Q2(R1) guideline (European Medicines Agency) as follows: DL = $3.3 \times \sigma/S$, where σ is estimated on the basis of the standard deviation of the ΔCurrent, and S is the slope of the linear fit from data we presented in Fig. 2d. The calculation was processed using OriginPro 2021 (OriginLab).

Calculation of the signal-to-noise ratio

In the case of thiosulfate sensing, the signal-to-noise ratio (SNR) was calculated as follows: SNR = μ/σ , where μ is the average signal strength, that is, the standard deviation of the ΔCurrent generated from bacteria, and σ is the standard deviation of the current. The average SNR across 150–400 min (Extended Data Fig. 4b) was calculated to reflect the SNR changes between planktonic (-gel) and encapsulated (+gel) strains.

Materials availability

Genetic constructs will be made available in Addgene and are available from the corresponding authors upon request.

Reporting summary

Further information on research design is available in the Nature Research Reporting Summary linked to this article.

Data availability

All data generated or analysed during this study are included in this published article and its Supplementary Information. Source data are provided with this paper.

42. Pinske, C., Bönn, M., Krüger, S., Lindenstrauss, U. & Sawers, R. G. Metabolic deficiencies revealed in the biotechnologically important model bacterium *Escherichia coli* BL21(DE3). *PLoS ONE* **6**, e22830 (2011).
43. Spiro, S. & Guest, J. R. Adaptive responses to oxygen limitation in *Escherichia coli*. *Trends Biochem. Sci.* **16**, 310–314 (1991).
44. Monk, J. M. et al. Multi-omics quantification of species variation of *Escherichia coli* links molecular features with strain phenotypes. *Cell Syst.* **3**, 238–251.e12 (2016).
45. Kim, H., Kim, S. & Yoon, S. H. Metabolic network reconstruction and genome analysis of the industrial microbe, *Escherichia coli* BL21(DE3). *PLoS ONE* **13**, e0204375 (2018).
46. Sauer, U., Canonaco, F., Heri, S., Perrenoud, A. & Fischer, E. The soluble and membrane-bound transhydrogenases UdhA and PntAB have divergent functions in NADPH metabolism of *Escherichia coli*. *J. Biol. Chem.* **279**, 6613–6619 (2004).
47. Fan, J. et al. Quantitative flux analysis reveals folate-dependent NADPH production. *Nature* **510**, 298–302 (2014).
48. Engler, C., Kandzia, R. & Marillonnet, S. A one pot, one step, precision cloning method with high throughput capability. *PLoS ONE* **3**, e3647 (2008).
49. Gibson, D. G. et al. Enzymatic assembly of DNA molecules up to several hundred kilobases. *Nat. Methods* **6**, 343–345 (2009).
50. Torella, J. P. et al. Unique nucleotide sequence-guided assembly of repetitive DNA parts for synthetic biology applications. *Nat. Protoc.* **9**, 2075–2089 (2014).
51. Bassalo, M. C. et al. Rapid and efficient one-step metabolic pathway integration in *E. coli*. *ACS Synth. Biol.* **5**, 561–568 (2016).
52. Datta, S., Costantino, N. & Court, D. L. A set of recombineering plasmids for gram-negative bacteria. *Gene* **379**, 109–115 (2006).
53. Zhang, Y. & Weiner, J. H. A simple semi-quantitative *in vivo* method using H₂S detection to monitor sulfide metabolizing enzymes. *Biotechniques* **57**, 208–210 (2014).
54. Fatin-Rouge, N., Starchev, K. & Buffle, J. Size effects on diffusion processes within agarose gels. *Biophys. J.* **86**, 2710–2719 (2004).

Acknowledgements *E. coli* EW11 and the genes encoding FNR and SIR were a gift from P. Silver (Harvard University). pSIM19 was a gift from D. Court (NIH-National Cancer Institute). pSS9 (Addgene, plasmid 71655), pSS9-RNA (Addgene, plasmid 71656) and pX2-Cas9 (Addgene, plasmid 8581) were gifts from R. Gill (University of Colorado). We thank S. Li (Rice University) for help with water sampling; X. Chen and C. Masiello (Rice University) with help with TOC

measurements; H. Du and D. Fu (Southeast University) with help with $\text{TiO}_2@\text{TiN}$ nanocomposite synthesis; J. Soman (Rice University) for internal reviewing and providing writing suggestions; and M. Baruch (Rice University) for helping to conceptualize the project. Funding was from the Office of Science, Office of Basic Energy Sciences of the US Department of Energy grants DE-SC0014462 (to J.J.S. and G.N.B.); Office of Naval Research grants 00014181P00037 (to C.M.A.-F.), N00014-17-1-2639 (to J.J.S.) and N00014-20-1-2274 (to C.M.A.-F. and J.J.S.); Cancer Prevention and Research Institute of Texas RR190063 (to C.M.A.-F.); National Science Foundation grant 1843556 (to J.J.S. and G.N.B.); Department of Energy Office of Science Graduate Student Research (SCGSR) Program Fellowship DE-SC0014664 (to J.T.A.); Loideska Stockbridge Vaughn Fellowship (to J.T.A.); and China Scholarship Council Fellowship CSC-201606090098 (to L.S.). Work at the Molecular Foundry was supported by the Office of Science, Office of Basic Energy Sciences, of the US Department of Energy under contract number DE-AC02-05CH11231.

Author contributions J.T.A., L.S., C.M.A.-F. and J.J.S. conceptualized the project. J.T.A. performed all molecular biology and genome engineering. J.T.A. and L.S. performed assays to verify the functions of the modules. L.S. and X.Z. developed the cell encapsulation protocol, performed the bioelectrochemical analysis of thiosulfate and 4-HT sensing, and performed

water sampling. L.S. synthesized the WO_3 and $\text{TiO}_2@\text{TiN}$ nanomaterials. X.Z. and C.M.A.-F. performed diffusion modelling. J.T.A., L.S. and X.Z. analysed and visualized all the data and made the schematic diagrams. J.T.A., L.S., X.Z., J.J.S. and C.M.A.-F. wrote the manuscript. All authors reviewed and edited the manuscript.

Competing interests J.J.S., J.T.A. and G.N.B. have submitted a patent application (number 16/186,226) covering the use of fragmented proteins as chemical-dependent electron carriers, entitled 'Regulating electron flow using fragmented proteins'. L.S., X.Z. and C.M.A.-F. declare no competing interests.

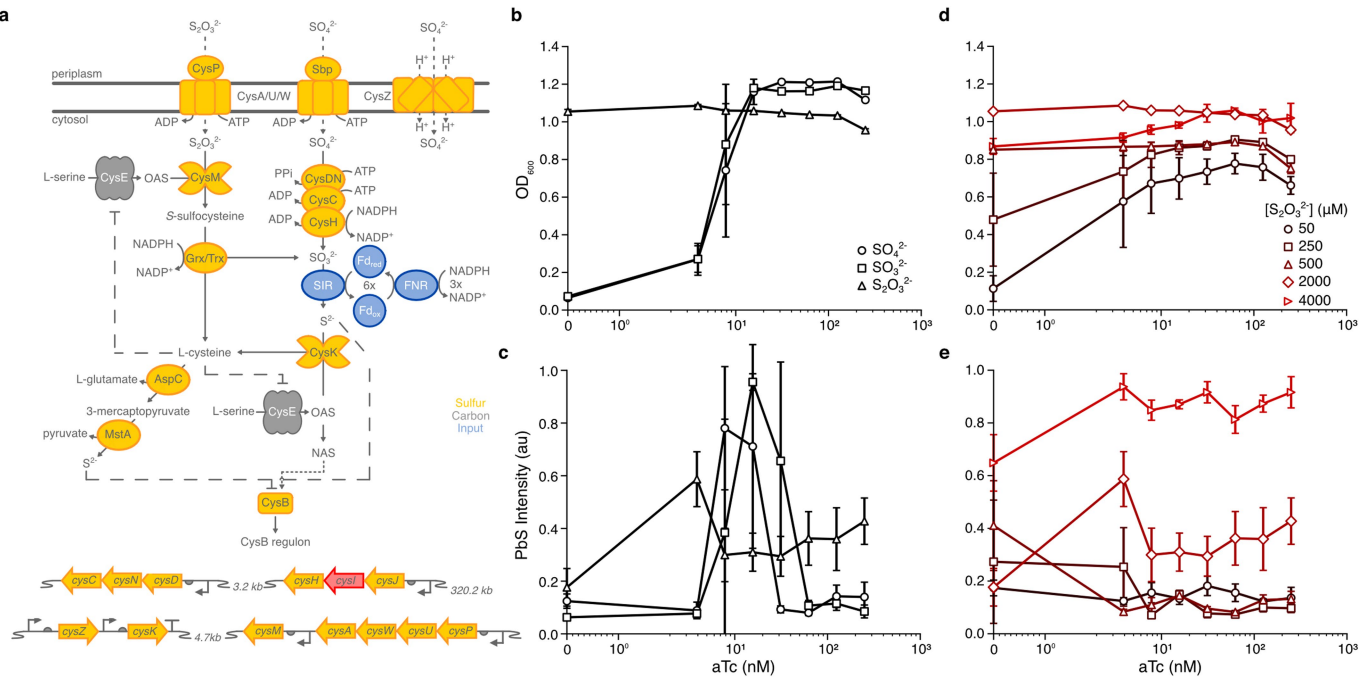
Additional information

Supplementary information The online version contains supplementary material available at <https://doi.org/10.1038/s41586-022-05356-y>.

Correspondence and requests for materials should be addressed to Jonathan J. Silberg or Caroline M. Ajo-Franklin.

Peer review information *Nature* thanks Luying Xun and the other, anonymous, reviewer(s) for their contribution to the peer review of this work. Peer reviewer reports are available.

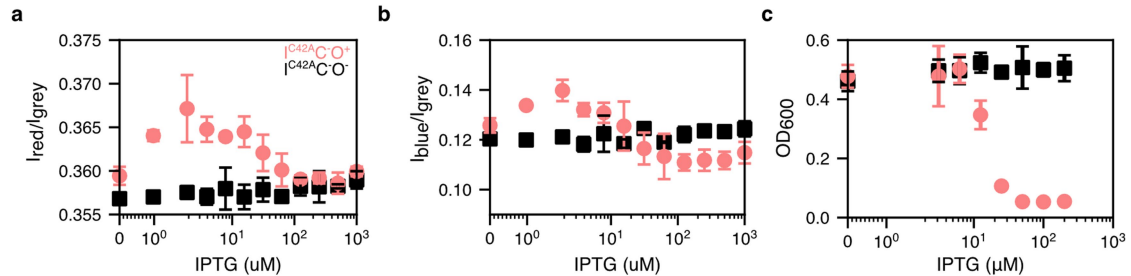
Reprints and permissions information is available at <http://www.nature.com/reprints>.



Extended Data Fig. 1 | Impact of sulfur source on sulfide evolution from *E. coli*

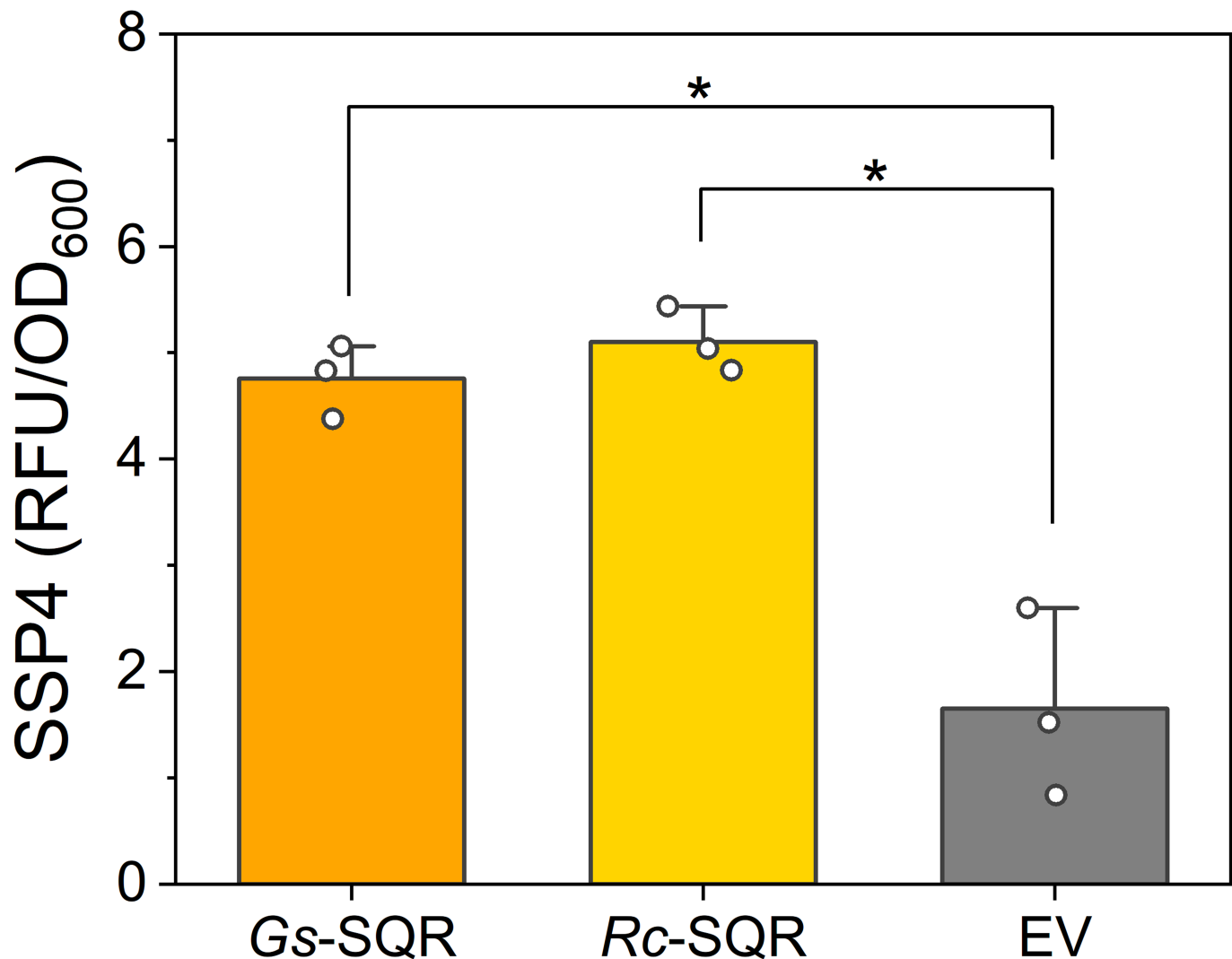
EW11. (A) A schematic of sulfur metabolism and regulation in *E. coli* (yellow) and the redox coupling of the Input module (blue) with this pathway. (B) PbS accumulation and (C) optical density of the I⁻C⁻O⁻ strain containing a vector for expressing Fd after 24 h in M9sa medium containing 2 mM of sulfate, sulfite, or thiosulfate and varying amounts of aTc to control Fd expression. The optical density in sulfate and sulfite containing media were significantly lower than thiosulfate containing media when < 7.81 nM aTc was added ($p = 8.47 \times 10^{-5}$ for 3.91 nM aTc with sulfate, $p = 6.98 \times 10^{-8}$ for 0 nM aTc with sulfate, $p = 1.70 \times 10^{-4}$

for for 3.91 nM aTc with sulfite, $p = 7.16 \times 10^{-8}$) for 0 nM aTc with sulfite. (D) PbS accumulation and (E) optical density after 24 h in M9sa medium containing varying amounts of thiosulfate and varying amounts of aTc to control Fd expression. In media with ≥ 0.25 mM thiosulfate, optical densities were not significantly different in the presence of aTc ($p > 0.01$ for all concentrations). For panels B-E, symbols and error bars represent the mean and standard deviation, respectively ($n = 3$ biologically independent samples). P-values were obtained using two-tailed, independent t-tests.



Extended Data Fig. 2 | Effect of Output module expression on cytochrome levels. (A) Red color intensity values of $I^{\text{C}^{42}\text{A}}\text{C}^-\text{O}^+$ (circle) or $I^{\text{C}^{42}\text{A}}\text{C}^-\text{O}^-$ (square) cell pellets following aerobic growth in 2xYT medium containing varying amounts of IPTG, which induces expression of CymA-MtrCAB. (B) Blue color intensity values of $I^{\text{C}^{42}\text{A}}\text{C}^-\text{O}^+$ (circle) or $I^{\text{C}^{42}\text{A}}\text{C}^-\text{O}^-$ (square) in minimal media containing lactate and electrochromic WO_3 nanoparticles that change from white to blue when reduced by microbes that present EET. (C) Cell density

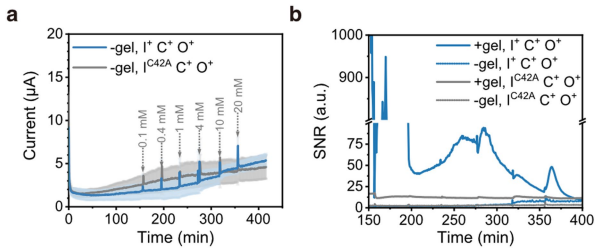
(OD₆₀₀) of $I^{\text{C}^{42}\text{A}}\text{C}^-\text{O}^+$ (circle) or $I^{\text{C}^{42}\text{A}}\text{C}^-\text{O}^-$ (square) grown in M9 minimal medium containing varying amounts of IPTG. Growth of $I^{\text{C}^{42}\text{A}}\text{C}^-\text{O}^+$ was significantly decreased at $>10 \mu\text{M}$ IPTG ($p = 6.55 \times 10^{-3}$ for $12.5 \mu\text{M}$, $p = 7.30 \times 10^{-6}$ for $25 \mu\text{M}$, $p = 3.87 \times 10^{-4}$ for $50 \mu\text{M}$, $p = 4.65 \times 10^{-6}$ for $100 \mu\text{M}$, $p = 5.89 \times 10^{-5}$ for $200 \mu\text{M}$). Data represents the mean values with error bars representing one standard deviation ($n = 3$ biologically independent samples). P-values were obtained using two-tailed, independent t-tests.

**Extended Data Fig. 3 | Sulfane sulfur accumulation in SQR expressing cells.**

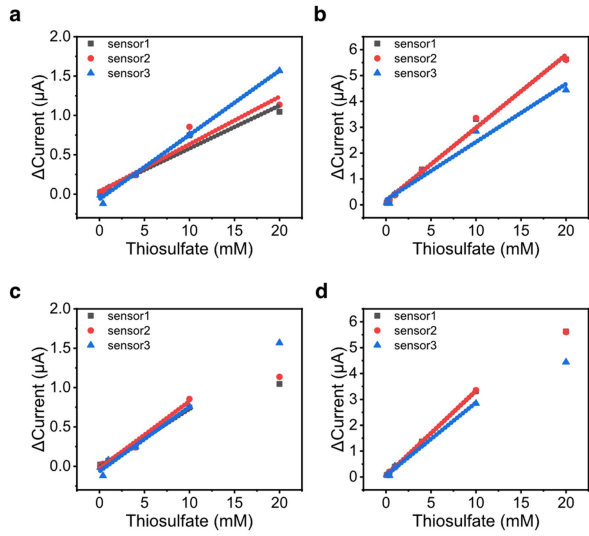
Relative fluorescence of cells treated with the sulfane sulfur probe SSP4.

The fluorescence from cells expressing *Gs*-SQR and *Rc*-SQR was significantly higher than cells transformed with an empty vector (EV) ($p = 4.89 \times 10^{-3}$ and $p = 3.14 \times 10^{-3}$, respectively). Fluorescence from cells expressing *Gs*-SQR and

Rc-SQR were not significantly different. Error bars represent one standard deviation ($n = 3$ biologically independent samples) with individual samples shown as white circles and bars heights representing the mean. P-values were obtained using two-tailed, independent t-tests.

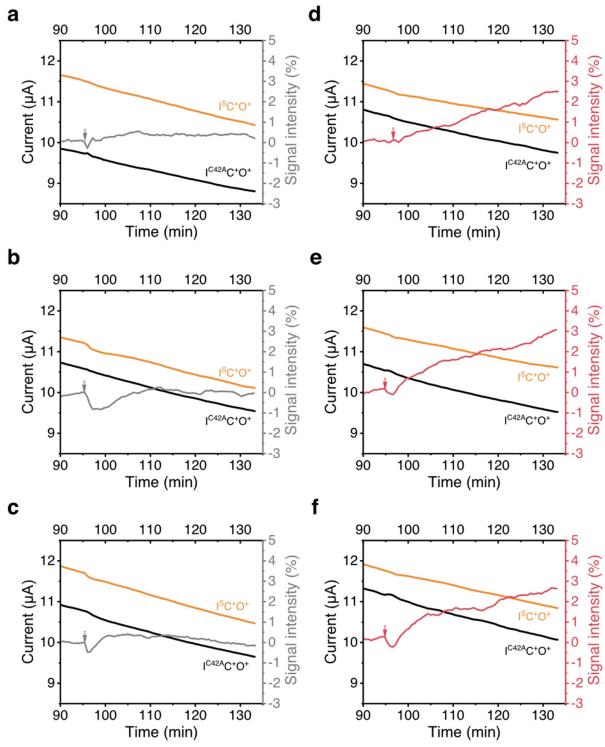


Extended Data Fig. 4 | Planktonic cells present a small, noisy current response to thiosulfate. (A) The chronoamperometric response of planktonic $I^3C^+O^+$ and $I^{C42A}C^+O^+$ cells in a bioelectrochemical reactor. Arrows indicate the addition of thiosulfate to varying concentrations. Data represents the mean values with error bars representing one standard deviation ($n = 3$ biologically independent samples). The working electrodes were poised at $+0.42 V_{SHE}$. (B) The signal-to-noise ratio (SNR) was calculated as dividing the average current generated from bacteria by the standard deviation ($n = 3$) of the current. The average SNR across the 150 to 400 min was calculated to reflect the SNR changes between planktonic (-gel) and encapsulated (+gel) strains, as 140.00 for $+gel, I^3C^+O^+$, 4.35 for $-gel, I^3C^+O^+$, 12.27 for $+gel, I^{C42A}C^+O^+$ and 2.88 for $-gel, I^{C42A}C^+O^+$.

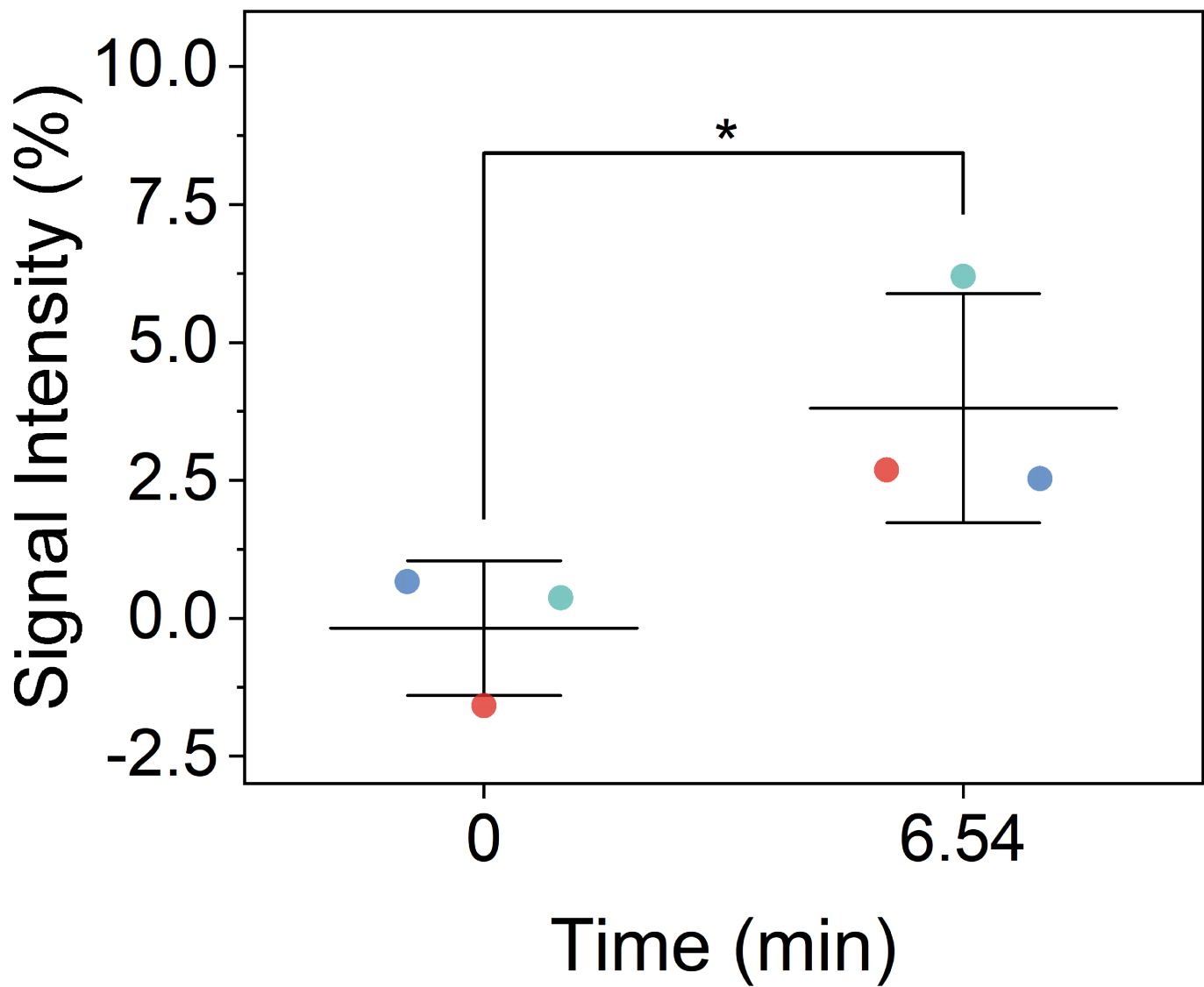


Extended Data Fig. 5 | Linear fit for the thiosulfate sensing with different

ranges. 5 min (A) and 30 min (B) sensing time, linear range from 0.1 mM to 20 mM; 5 min (C) and 30 min (D) sensing time, linear range from 0.1 mM to 10 mM.

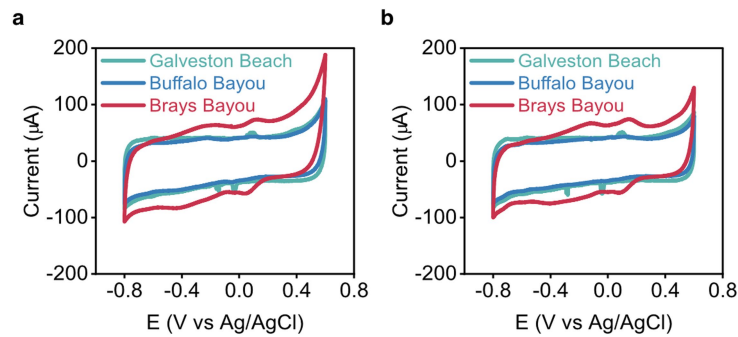


Extended Data Fig. 6 | Amperometric response and calculated signal intensity of $\text{I}^{15\text{C}^+}\text{O}^+$ and $\text{I}^{142\text{A}}\text{C}^+\text{O}^+$ upon addition of DMSO (A, B, C) or 4-HT (D, E, F) in each 2-EWE configured BES with working electrodes poised at +0.42 V_{SHE}. Time zero indicates the start of the chronoamperometric measurements.



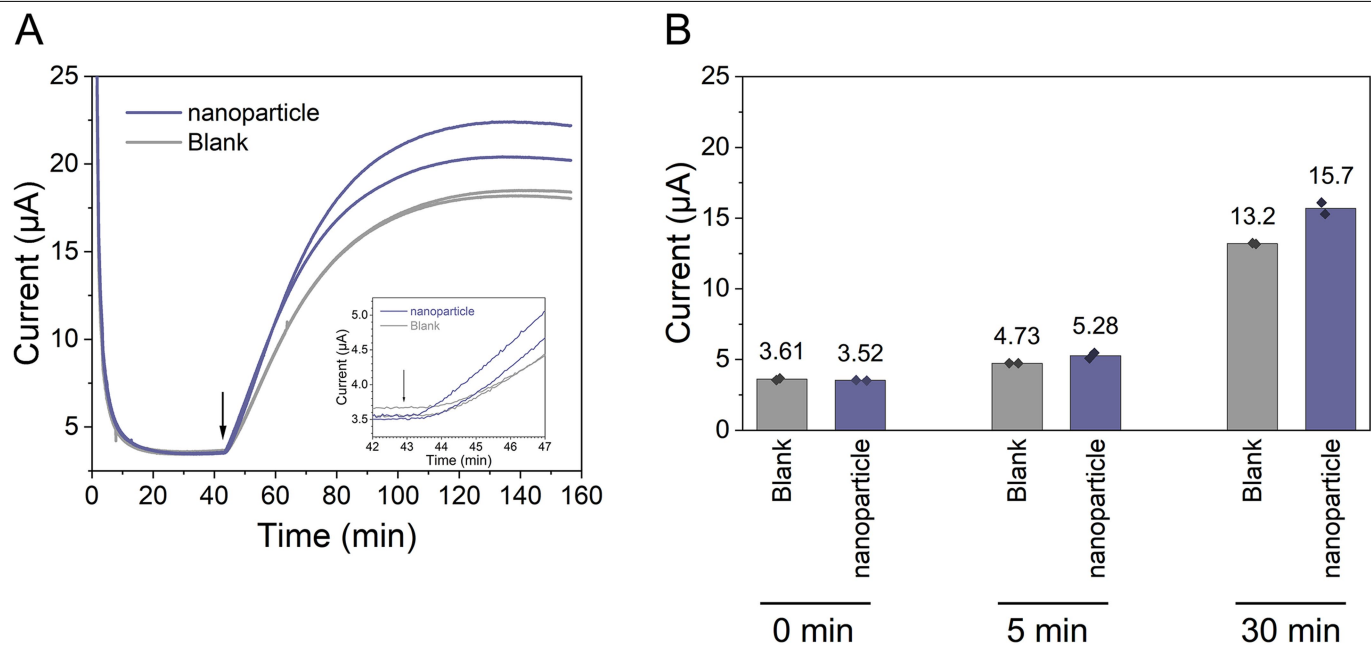
Extended Data Fig. 7 | Response of $I^+C^+O^+$ and $I^{C42A}C^+O^+$ to thiosulfate in complex urban waterway samples. Percent increase in the amperometric response of $I^+C^+O^+$ relative to $I^{C42A}C^+O^+$ immediately before and 6.54 min ($p = 0.045$) after addition of 10 mM thiosulfate in the waterway samples from

Brays Bayou (red), Buffalo Bayou (blue), and Galveston Beach (green). Each point represents a single waterway replicate, the center line represents the mean of the response in the three waterway samples with error bars representing one standard deviation.



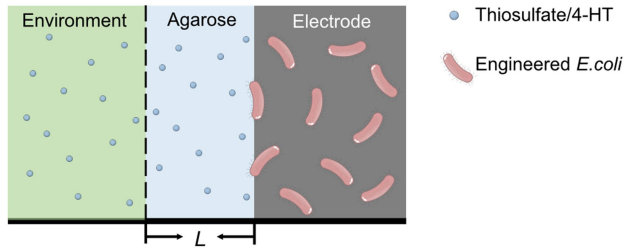
Extended Data Fig. 8 | Cyclic voltammetry analysis of environmental samples. (A) Each environmental sample shows multiple pairs of redox peaks, indicating abundant redox active chemicals exist which might interfere with

4-HT sensing. (B) Environmental samples supplemented with 0.2% glucose show no changes to their voltammograms. All CVs were measured at a scan rate of 10 mV/s.



Extended Data Fig. 9 | Addition of $\text{TiO}_2@\text{TiN}$ nanoparticles enables more current collection. (A) Chronoamperometry and (B) current of $\text{I}^-\text{C}^+\text{O}^+$ strain encapsulated in an alginate-agarose hydrogel with and without $\text{TiO}_2@\text{TiN}$ nanoparticles upon addition of 1 mM thiosulfate (arrow). The strains

encapsulated with nanoparticles respond to thiosulfate more rapidly and with a higher steady-state level. Data represents two biologically independent measurements.



Extended Data Fig. 10 | Simplified 1D geometry for calculation of diffusion timescales for the response of the living bioelectronic sensor. Schematic of analyte diffusion from bulk solution through the agarose layer to cells embedded in the hydrogel on the electrode surface.

Reporting Summary

Nature Portfolio wishes to improve the reproducibility of the work that we publish. This form provides structure for consistency and transparency in reporting. For further information on Nature Portfolio policies, see our [Editorial Policies](#) and the [Editorial Policy Checklist](#).

Statistics

For all statistical analyses, confirm that the following items are present in the figure legend, table legend, main text, or Methods section.

n/a Confirmed

- The exact sample size (n) for each experimental group/condition, given as a discrete number and unit of measurement
- A statement on whether measurements were taken from distinct samples or whether the same sample was measured repeatedly
- The statistical test(s) used AND whether they are one- or two-sided
 - Only common tests should be described solely by name; describe more complex techniques in the Methods section.*
- A description of all covariates tested
- A description of any assumptions or corrections, such as tests of normality and adjustment for multiple comparisons
- A full description of the statistical parameters including central tendency (e.g. means) or other basic estimates (e.g. regression coefficient) AND variation (e.g. standard deviation) or associated estimates of uncertainty (e.g. confidence intervals)
- For null hypothesis testing, the test statistic (e.g. F , t , r) with confidence intervals, effect sizes, degrees of freedom and P value noted
 - Give P values as exact values whenever suitable.*
- For Bayesian analysis, information on the choice of priors and Markov chain Monte Carlo settings
- For hierarchical and complex designs, identification of the appropriate level for tests and full reporting of outcomes
- Estimates of effect sizes (e.g. Cohen's d , Pearson's r), indicating how they were calculated

Our web collection on [statistics for biologists](#) contains articles on many of the points above.

Software and code

Policy information about [availability of computer code](#)

Data collection Electrochemical data were collected using EC-lab (version 11.36); Sulfide consumption data were collected using UniSense SensorTrace (version 3.2.0.25423), Microplate growth data were collected using Tecan SparkControl (version 2.1)

Data analysis OriginPro 2021b (64-bit) SR2 (version 9.8.5.212) was used to plot and analyse the data; Python 3.7.9, Matplotlib 3.3.2, and SciPy 1.5.2 were used to plot and analyse data; Matlab (version R2018a) was used for image color analysis of bacterial pellet and WO₃ nanoparticle images; FIJI (version 1.53c) and ReadPlate3 plugin were used for color analysis of lead acetate paper images. ZView 3.5b was used to analyze electrochemical impedance spectroscopy data.

For manuscripts utilizing custom algorithms or software that are central to the research but not yet described in published literature, software must be made available to editors and reviewers. We strongly encourage code deposition in a community repository (e.g. GitHub). See the Nature Portfolio [guidelines for submitting code & software](#) for further information.

Data

Policy information about [availability of data](#)

All manuscripts must include a [data availability statement](#). This statement should provide the following information, where applicable:

- Accession codes, unique identifiers, or web links for publicly available datasets
- A description of any restrictions on data availability
- For clinical datasets or third party data, please ensure that the statement adheres to our [policy](#)

All data generated or analyzed during this study are included in this published article (and its supplementary information files).

Field-specific reporting

Please select the one below that is the best fit for your research. If you are not sure, read the appropriate sections before making your selection.

- Life sciences Behavioural & social sciences Ecological, evolutionary & environmental sciences

For a reference copy of the document with all sections, see nature.com/documents/nr-reporting-summary-flat.pdf

Life sciences study design

All studies must disclose on these points even when the disclosure is negative.

Sample size	Sample size was determined in accordance with community standards. All experiments were performed in triplicate (n=3) except for Figure 4C due to limited environmental samples.
Data exclusions	No data were excluded from analyses.
Replication	All replication attempts in this study were successful
Randomization	All bacterial cell cultures used for each experiments were grown under the same conditions, so randomization was not relevant
Blinding	This study only provides objective measurements of samples derived from bacterial cultures subjected to identical growth conditions per experiment. Blinding was not relevant for this study

Reporting for specific materials, systems and methods

We require information from authors about some types of materials, experimental systems and methods used in many studies. Here, indicate whether each material, system or method listed is relevant to your study. If you are not sure if a list item applies to your research, read the appropriate section before selecting a response.

Materials & experimental systems		Methods	
n/a	Involved in the study	n/a	Involved in the study
<input checked="" type="checkbox"/>	<input type="checkbox"/> Antibodies	<input checked="" type="checkbox"/>	<input type="checkbox"/> ChIP-seq
<input checked="" type="checkbox"/>	<input type="checkbox"/> Eukaryotic cell lines	<input checked="" type="checkbox"/>	<input type="checkbox"/> Flow cytometry
<input checked="" type="checkbox"/>	<input type="checkbox"/> Palaeontology and archaeology	<input checked="" type="checkbox"/>	<input type="checkbox"/> MRI-based neuroimaging
<input checked="" type="checkbox"/>	<input type="checkbox"/> Animals and other organisms		
<input checked="" type="checkbox"/>	<input type="checkbox"/> Human research participants		
<input checked="" type="checkbox"/>	<input type="checkbox"/> Clinical data		
<input checked="" type="checkbox"/>	<input type="checkbox"/> Dual use research of concern		